photonics

MDPI

Article

Polarimeter Optical Spectrum Analyzer

Eyal Buks

Andrew and Erna Viterbi Department of Electrical Engineering, Technion—Israel Institute of Technology, Haifa 32000, Israel; eyal@ee.technion.ac.il

Abstract: A coherent optical spectrum analyzer is integrated with a rotating quarter wave plate polarimeter. The combined polarimeter optical spectrum analyzer (POSA) allows the extraction of the state of polarization with high spectral resolution. The POSA is used in this work to study two optical systems. The first is an optical modulator based on a ferrimagnetic sphere resonator. The POSA is employed to explore the underlying magneto–optical mechanism responsible for modulation sideband asymmetry. The second system under study is a cryogenic fiber loop laser, which produces an unequally spaced optical comb. The polarization measurements provide insights into the nonlinear processes responsible for comb creation. Characterizations extracted from the POSA data provide guidelines for the performance optimization of applications based on the systems under study.

Keywords: ferrimagnetic sphere resonator; cryogenic fiber loop laser

1. Introduction

The optical state of polarization (SOP) can be measured using a variety of techniques [1]. For some applications, the dependency of the SOP on the optical wavelength λ has to be determined. This dependency on λ can be obtained by combining a wavelength tunable band-pass optical filter with the polarimeter being used to measure the SOP. This relatively simple configuration has a spectral resolution that is limited by the ratio between the filter's free spectral range (FSR) and its finesse. Lowering the spectral resolution below about 1 GHz over a wide tuning range in the optical band is practically challenging. On the other hand, for some applications, a much higher spectral resolution is needed.

A coherent optical spectrum analyzer (OSA) [2–4] is an instrument based on the heterodyne detection of the optical signal under study [5–7]. Commonly, a coherent OSA has significantly higher spectral resolution compared to a grating-based OSA. In its standard configuration, the SOP cannot be extracted from coherent OSA data. In this work a fiber-based system is proposed, which integrates a coherent OSA with a polarimeter (PM) that is based on a rotating quarter wave plate (RQWP). The integrated polarimeter optical spectrum analyzer (POSA) allows determining both the SOP and the degree of polarization (DOP) with high spectral resolution.

The SOP can be described as a point in the Poincaré unit sphere (see Figure 1a). The colinear vertical, horizontal, diagonal, and anti-diagonal SOP are denoted by $|V\rangle$, $|H\rangle$, $|D\rangle = 2^{-1/2}(|H\rangle + |V\rangle)$, and $|A\rangle = 2^{-1/2}(|H\rangle - |V\rangle)$, respectively, whereas the circular right-hand and left-hand SOP are denoted by $|R\rangle = 2^{-1/2}(|H\rangle - i|V\rangle)$ and $|L\rangle = 2^{-1/2}(|H\rangle + i|V\rangle)$, respectively. The unit vectors in the Poincaré sphere corresponding to the SOP $|V\rangle$, $|H\rangle$, $|D\rangle$, $|A\rangle$, $|R\rangle$ and $|L\rangle$, are $\hat{\mathbf{x}}_3$, $-\hat{\mathbf{x}}_3$, $\hat{\mathbf{x}}_1$, $-\hat{\mathbf{x}}_1$, $-\hat{\mathbf{x}}_2$, and $\hat{\mathbf{x}}_2$, respectively.

In this work, the POSA is employed for studying two systems. The first is a ferrimagnetic sphere resonator (FMSR) made of yttrium iron garnet (YIG) (see Sections 3 and 4). It has been recently demonstrated that optical single sideband modulation (SSM) can be implemented in the telecom band using an FMSR [8,9]. Section 5 is devoted to POSA measurements of a cryogenic fiber loop laser, which is operated in a region where an unequally spaced optical comb (USOC) is formed [10]. For both systems, the theoretical interpretation of the POSA measurement results is discussed.

check for updates

Citation: Buks, E. Polarimeter Optical Spectrum Analyzer. *Photonics* **2024**, *11*, 486. https://doi.org/10.3390/photonics11060486

Received: 26 March 2024
Revised: 12 May 2024
Accepted: 19 May 2024
Published: 21 May 2024

Copyright: © 2024 by the author. Licensee MDPI, Basel, Switzerland. This article is an open access article distributed under the terms and conditions of the Creative Commons Attribution (CC BY) license (https://creativecommons.org/licenses/by/4.0/).

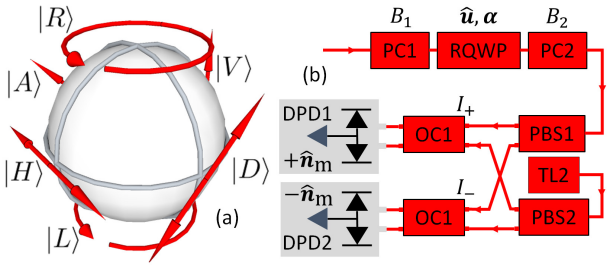


Figure 1. SOP. (**a**) The Poincaré sphere. (**b**) The POSA setup.

2. POSA

The POSA setup is schematically shown in Figure 1b. The input section contains two polarization controllers (PC1 and PC2 in Figure 1b) and an RQWP (which is based on a rotating stage placed between two fiber collimators). Heterodyne detection in the coherent OSA section is performed using a wavelength tunable laser (TL2 in Figure 1b), two polarized beam splitters (PBS1 and PBS2 in Figure 1b), two 50:50 optical couplers (OC1 and OC2 in Figure 1b), and two differential photodetectors (DPD1 and DPD2 in Figure 1b).

In some other RQWP-based polarimeters, the RQWP is directly attached to a PBS and a photodetector [1]. In contrast, a single mode fiber is used in our setup to connect the RQWP to the coherent OSA section (see Figure 1b). This inter-section connection gives rise to a unitary transformation denoted by B_2. The transformation B_2 can be manipulated using PC2; however, it is a priori unknown. Consequently, the extraction process of the SOP from the POSA data, which is explained below, is more complicated than the process that is commonly employed in other RQWP-based polarimeters, for which B_2 represents the identity transformation [1].

Let ρ be the density matrix of a given SOP, and let P_m be the matrix representation of a given projection operator (associated with a given polarization filter). The 2×2 matrices ρ and P_m are expressed as $\rho = (1/2)(1 + \gamma \hat{\mathbf{n}} \cdot \boldsymbol{\sigma})$ and $P_\mathrm{m} = (1/2)(1 + \hat{\mathbf{n}}_\mathrm{m} \cdot \boldsymbol{\sigma})$, where both $\hat{\mathbf{n}} = \gamma^{-1}(P_1, P_2, P_3) = (\sin\theta_\mathrm{n} \cos\varphi_\mathrm{n}, \cos\theta_\mathrm{n}, \sin\theta_\mathrm{n} \sin\varphi_\mathrm{n})$ and $\hat{\mathbf{n}}_\mathrm{m} = (m_1, m_2, m_3) = (\sin\theta \cos\varphi, \cos\theta, \sin\theta \sin\varphi)$ are real unit vectors (the over-hat symbol is used to denote unit vectors), $0 \leq \gamma \leq 1$ is the DOP, and $\boldsymbol{\sigma} = (\sigma_1, \sigma_2, \sigma_3)$ is the Pauli matrix vector

$$\sigma_1 = \begin{pmatrix} 0 & 1 \\ 1 & 0 \end{pmatrix}, \ \sigma_2 = \begin{pmatrix} 0 & -i \\ i & 0 \end{pmatrix}, \ \sigma_3 = \begin{pmatrix} 1 & 0 \\ 0 & -1 \end{pmatrix}. \tag{1}$$

Using the relation $(\boldsymbol{\sigma} \cdot \mathbf{a})(\boldsymbol{\sigma} \cdot \mathbf{b}) = \mathbf{a} \cdot \mathbf{b} + i\boldsymbol{\sigma} \cdot (\mathbf{a} \times \mathbf{b})$, one finds that the probability p to determine the SOP pointing in the $\hat{\mathbf{n}}_\mathrm{m}$ direction is given by

$$p = \mathrm{Tr}(\rho P_\mathrm{m}) = \frac{1 + \gamma \hat{\mathbf{n}} \cdot \hat{\mathbf{n}}_\mathrm{m}}{2}. \tag{2}$$

While the unit vector $\hat{\mathbf{n}}_\mathrm{m}$ is associated with the polarization filter of OSA trace 1 (DPD1), OSA trace 2 (DPD2) represents the orthogonal SOP corresponding to the unit vector $-\hat{\mathbf{n}}_\mathrm{m}$. For a given input signal having intensity I, the OSA trace 1 (2) signal intensity I_+ (I_-) is given by $I_\pm / I = (1/2)(1 \pm \gamma \hat{\mathbf{n}} \cdot \hat{\mathbf{n}}_\mathrm{m})$ [see Equation (2)], and thus the following holds

$$\gamma \hat{\mathbf{n}} \cdot \hat{\mathbf{n}}_\mathrm{m} = \frac{I_+ - I_-}{I_+ + I_-}. \tag{3}$$

Any loss-less linear SOP transformation can be described using a unitary Jones matrix $B(\hat{\mathbf{u}}, \phi)$ given by [11]

$$B(\hat{\mathbf{u}}, \phi) \doteq \exp\left(-\frac{i\,\boldsymbol{\sigma} \cdot \hat{\mathbf{u}} \phi}{2}\right) = \mathbf{1} \cos\frac{\phi}{2} - i\boldsymbol{\sigma} \cdot \hat{\mathbf{u}} \sin\frac{\phi}{2}, \tag{4}$$

where $\hat{\mathbf{u}}$ is a unit vector, and ϕ is a rotation angle. By expressing the unit vector $\hat{\mathbf{n}}$ as $\hat{\mathbf{n}} = \mathbf{n}_{\parallel} + \mathbf{n}_{\perp}$, where $\mathbf{n}_{\parallel} = (\hat{\mathbf{u}} \cdot \hat{\mathbf{n}})\hat{\mathbf{u}}$ (parallel component of $\hat{\mathbf{n}}$ in the $\hat{\mathbf{u}}$ direction), and $\mathbf{n}_{\perp} = \hat{\mathbf{u}} \times (\hat{\mathbf{n}} \times \hat{\mathbf{u}})$ (perpendicular component), one finds that

$$B(\hat{\mathbf{u}}, \phi)(\sigma \cdot \hat{\mathbf{n}})B^{\dagger}(\hat{\mathbf{u}}, \phi) = \sigma \cdot \hat{\mathbf{n}}_{\mathrm{T}} \,, \tag{5}$$

where

$$\hat{\mathbf{n}}_{\mathrm{T}} = \mathbf{n}_{\parallel} + \mathbf{n}_{\perp} \cos\phi + (\hat{\mathbf{u}} \times \mathbf{n}_{\perp}) \sin\phi \,. \tag{6}$$

The transformation from $\hat{\mathbf{n}}$ to $\hat{\mathbf{n}}_{\mathrm{T}}$ (6) is a rotation about the $\hat{\mathbf{u}}$ axis with angle ϕ.

The unit vector $\hat{\mathbf{u}}$ corresponding to the RQWP is given by $\hat{\mathbf{u}} = -\sin(2\alpha)\hat{\mathbf{x}}_1 + \cos(2\alpha)\hat{\mathbf{x}}_3$, where α is the RQWP axis angle, and the rotation angle ϕ is given by $\phi = \pi/2$; thus, we have (see Equations (5) and (6))

$$\begin{aligned} \gamma \hat{\mathbf{n}}_{\mathrm{T}} \cdot \hat{\mathbf{n}}_{\mathrm{m}} &= \gamma((\hat{\mathbf{u}} \cdot \hat{\mathbf{n}})\hat{\mathbf{u}} + (\hat{\mathbf{u}} \times \mathbf{n})) \cdot \hat{\mathbf{n}}_{\mathrm{m}} \\ &= a_0 + a_1 \cos(2\alpha) + b_1 \sin(2\alpha) \\ &+ a_2 \cos(4\alpha) + b_2 \sin(4\alpha) \,, \end{aligned} \tag{7}$$

where

$$a_0 = \frac{P_1 m_1 + P_3 m_3}{2} \,, \tag{8}$$

$$a_1 = P_1 m_2 - P_2 m_1 \,, \tag{9}$$

$$b_1 = P_3 m_2 - P_2 m_3 \,, \tag{10}$$

$$a_2 = \frac{P_3 m_3 - P_1 m_1}{2} \,, \tag{11}$$

$$b_2 = -\frac{P_1 m_3 + P_3 m_1}{2} \,. \tag{12}$$

The following holds (see Equations (11) and (12)):

$$a_2^2 + b_2^2 = \frac{\gamma^2 \sin^2\theta \sin^2\theta_{\mathrm{n}}}{4} \,. \tag{13}$$

The Poincaré vector $\mathbf{P} = (P_1, P_2, P_3)$ can be extracted from Equations (8)–(12), and the measured values of a_0, a_1, b_1, a_2, and b_2, provided that the transformation B_2, which determines the unit vector $\hat{\mathbf{n}}_{\mathrm{m}} = (m_1, m_2, m_3)$, is given. The POSA calibration (which is needed because B_2 is a priori unknown) is performed by varying the angles θ_{n} and φ_{n} associated with the SOP transformation B_1 controlled by PC1, while keeping θ and φ unchanged (θ and φ are determined by the SOP transformation B_2 from the RQWP to the coherent OSA section, which can be manipulated using PC2). This process allows determining the angle θ_{n} using the relation (see Equation (13))

$$\sin^2\theta_{\mathrm{n}} = \frac{a_2^2 + b_2^2}{\max_{\theta_{\mathrm{n}}, \varphi_{\mathrm{n}}}(a_2^2 + b_2^2)} \,. \tag{14}$$

The unit vector $\hat{\mathbf{n}}_{\mathrm{m}} = (\sin\theta\cos\varphi, \cos\theta, \sin\theta\sin\varphi)$ can be manipulated by PC2 (see Figure 1b). As can be seen from Equation (13), the angle θ can be tuned such that $\sin^2\theta = 1$, by maximizing $a_2^2 + b_2^2$ using PC2. For this case, $a_1^2 + b_1^2 + 4(a_2^2 + b_2^2) = \gamma^2$. This PC2 calibration, which greatly simplifies the SOP extraction from the POSA data, has been performed prior to all measurements with both a driven FMSR (Sections 3 and 4) and with a cryogenic fiber loop laser (Section 5).

3. FMSR Modulator

FMSRs are widely employed as magnetically tunable microwave filters having high-quality factors. The FMSR ellipsoidal shape allows uniform magnetization. Magneto–optical (MO) coupling [12–20] between the FMSR optical [21–23] and magnetic Walker [24] modes can be used for implementing optical modulation [8,9,25–35]. The sequence of side-

bands that are generated in an FMSR-based modulator can be determined from Brillouin scattering selection rules [8,25–27,29–31,36–40], and angular momentum conservation in photon–magnon scattering [41–47]. Contrary to some other modulation techniques (such as amplitude, phase, and frequency modulations) [48–50], the symmetry between Stokes and anti-Stokes sidebands can be broken in FMSR-based modulation [8,9,35]. In particular, the method of single sideband modulation (SSM), which allows reducing both the transmission power and bandwidth, can be implemented using FMSR modulation.

The FMSR modulator is schematically shown in Figure 2a. An FMSR made of YIG having radius of $R_s = 125\,\mu m$ is held by two ceramic ferrules (CF). The two CFs, which are held by a concentric sleeve, provide transverse alignment for both input and output single mode optical fibers. All optical measurements are performed in the telecom band, in which YIG has a refractive index of 2.19 and an absorption coefficient of $(0.5\,m)^{-1}$ [51]. The intensity and SOP of light illuminating the FMSR are controlled by an optical attenuator (Att) and a PC, respectively. The blue-colored microwave (MW) components shown in Figure 2a allow both driving and detection of FMSR magnetic resonances. The FMSR is inductively coupled to a microwave loop antenna (MWA). Magnetic resonances are identified using a vector network analyzer (VNA). A signal generator (SG) is employed for driving, and the response is monitored using a radio frequency spectrum analyzer (RFSA). A circulator (C) and a splitter (S) are employed to direct the input and output microwave signals (see Figure 2a).

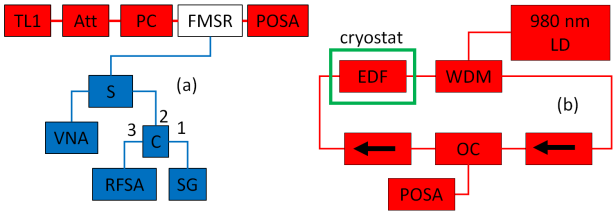


Figure 2. Experimental setup. Optical components and fibers are in red, whereas blue is used to label the MW components and coaxial cables. (**a**) Optical fibers are installed on both sides of the FMSR for transmission of light through the sphere (see Ref. [35] for more details on the experimental setup). (**b**) The cryogenic fiber loop laser (see Ref. [52] for more details).

The angular frequency of the FMSR Kittel mode ω_m is approximately given by $\omega_m = \mu_0 \gamma_e H_s$, where H_s is the static magnetic field, μ_0 is the free space permeability, and $\gamma_e/2\pi = 28\,GHzT^{-1}$ is the gyromagnetic ratio [20,53–55]. The applied static magnetic field $\mathbf{H}_s$ is controlled by adjusting the relative position of a magnetized Neodymium using a motorized stage. The static magnetic field $\mathbf{H}_s$ is normal to the unit vector $\hat{\mathbf{k}}$ pointing in the light propagation direction, and the MWA driving magnetic field is nearly parallel to $\hat{\mathbf{k}}$. The FMSR is installed such that its crystallographic direction [111] is aligned to $\hat{\mathbf{k}}$.

The plot in Figure 3(2) shows the POSA DPD1 signal intensity (see Figure 1b) as a function of TL2 optical wavelength λ. For this plot, the TL1 (see Figure 2a) power is $P_L = 6\,mW$, and the wavelength is $\lambda_L = 1537.7\,nm$. The MWA driving, which has a power of 12 dBm, is frequency tuned to the resonance at $\omega_m/(2\pi) = 4.1755\,GHz$. The driving-induced sidebands around the central peak (see Figure 3(2)) have wavelengths $\lambda_L(1 \pm \lambda_L \omega_m/(2\pi c)) = \lambda_L \pm 32.9\,pm$, where c is the vacuum speed of light. The sidebands' intensities strongly depend on the input light SOP. This dependency is explored in the next section, which is devoted to the FMSR transverse dielectric tensor.

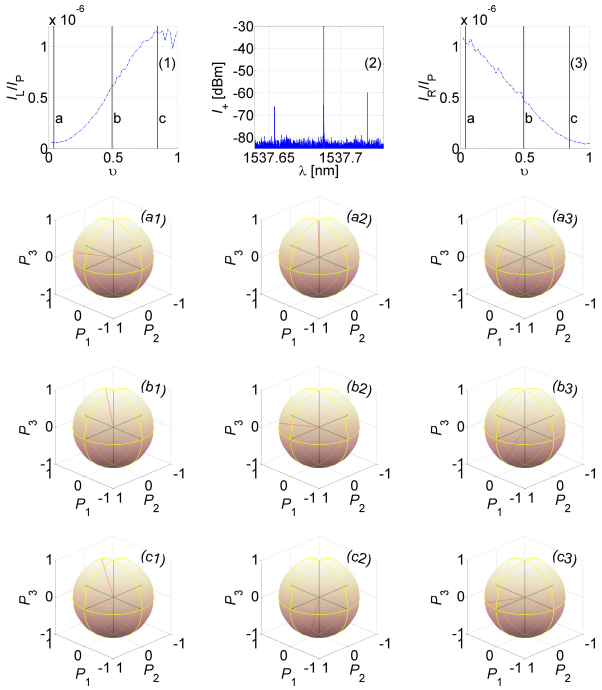


Figure 3. FMSR. Normalized sideband intensities $I_{\mathrm{L}}/I_{\mathrm{P}}$ and $I_{\mathrm{R}}/I_{\mathrm{P}}$ are shown in (**1**) and (**3**), respectively (I_{P} is the central peak intensity). The letters a, b, and c in the Poincaré plots' labels refer to the values of v indicated in (**1**) and (**3**). The numbers 1, 2, and 3 in the Poincaré plots' labels refer to the left sideband, central peak, and right sideband, respectively. The Poincaré vectors are shown in red.

4. FMSR Transverse Dielectric Tensor

In a Cartesian coordinate system, for which the [100], [010], and [001] crystallographic directions are pointing in the x, y and z axes, respectively, the dielectric tensor is represented by a 3×3 matrix denoted by ε [56–58]. The Onsager reciprocal relations, which originate from time-reversal symmetry, read $\epsilon_{nm}(\mathbf{M}) = \epsilon_{mn}(-\mathbf{M})$, where $\mathbf{M} = (M_1, M_2, M_3)$ is the magnetization vector, and $n, m \in \{1, 2, 3\}$. The MO Stoner–Wohlfarth energy density is given by $u = (1/4)\mathbf{E}^* \varepsilon \mathbf{E}^{\mathrm{T}}$, where $\mathbf{E} = (E_1, E_2, E_3)$ is the electric field vector phasor.

For the second order in the magnetization $\mathbf{M}$, the dielectric tensor can be expressed as $\varepsilon = \varepsilon_{\mathrm{r}} + \varepsilon_1 + \varepsilon_2$, where ε_{r} is the relative permittivity. The first order (in $\mathbf{M}$) contribution to the dielectric tensor is given by $\varepsilon_1 = iQ_{\mathrm{s}}\epsilon_{ijk}M_k$, where ϵ_{ijk} is the Levi–Civita symbol. For YIG in saturated magnetization, $Q_{\mathrm{s}} \simeq 10^{-4}$ [59]. The crystal cubic symmetry implies that the second order contribution ε_2 can be expressed as $\varepsilon_2 = g\,\mathrm{diag}(M_1^2, M_2^2, M_3^2) + g_{12}\mathbf{M}\mathbf{M}^{\mathrm{T}} + 2g_{44}\mathbf{M}^{\mathrm{T}}\mathbf{M}$, where g, g_{12}, and g_{44} are constants [60,61] (in the notation used in Ref. [60] $g = g_{11} - g_{12} - 2g_{44}$).

Consider the coordinate transformation $\mathbf{M}' = \mathbf{M}\mathcal{R}$, where $\mathcal{R}$ is a 3×3 rotation matrix. The energy density can be expressed as $u = (1/4)\mathbf{E}'^* \varepsilon' \mathbf{E}'^{\mathrm{T}}$, where $\mathbf{E}' = \mathbf{E}\mathcal{R}$ is the transformed value of the electric field $\mathbf{E}$, and where $\varepsilon' = \mathcal{R}^{-1}\varepsilon\mathcal{R}$ is the transformed value of the dielectric tensor ε (note that $\mathcal{R}^{\mathrm{T}} = \mathcal{R}^{-1}$ and that $\mathcal{R}$ is real). The corresponding transformed first- (second-) order contribution to the dielectric tensor is denoted by ε_1' (ε_2').

The following holds: $\mathbf{E}^* \varepsilon_1 \mathbf{E}^{\mathrm{T}} = -iQ_{\mathrm{s}}\mathbf{E}^* \cdot (\mathbf{M} \times \mathbf{E})$; thus, using the matrix identity $(\mathcal{R}\mathbf{X}) \times (\mathcal{R}\mathbf{Y}) = \mathcal{R}(\mathbf{X} \times \mathbf{Y})$, where $\mathbf{X}$ and $\mathbf{Y}$ are vectors, and $\mathcal{R}$ is a rotation matrix, one finds that $\varepsilon_1'(\mathbf{M}') = \varepsilon_1(\mathbf{M})$, i.e., $\varepsilon_1' = iQ_{\mathrm{s}}\epsilon_{ijk}M_k'$. The transformed second-order contribution ε_2' is given by $\varepsilon_2' = gE_{\mathrm{g}}' + g_{12}\mathbf{M}'(\mathbf{M}')^{\mathrm{T}} + 2g_{44}(\mathbf{M}')^{\mathrm{T}}\mathbf{M}'$, where

$$E_{\mathrm{g}}' = \sum_{n=1}^{3} \mathcal{R}^{-1}\eta_{n,n}\mathcal{R}\,(\mathbf{M}')^{\mathrm{T}}\mathbf{M}'\mathcal{R}^{-1}\eta_{n,n}\mathcal{R}\,, \tag{15}$$

and where $\eta_{n,m}$ is a 3×3 matrix, whose entries are given by $(\eta_{n,m})_{n',m'}=\delta_{n,n'}\delta_{m,m'}$. Note that only the term $E'_{\rm g}$ given by Equation (15) gives rise to the dependency of ε'_2 on the crystallographic directions.

The rotation matrix $\mathcal{R}$, which is given by

$$\mathcal{R}=\begin{pmatrix} \frac{\cos\phi}{\sqrt{2}}-\frac{\sin\phi}{\sqrt{6}} & -\frac{\cos\phi}{\sqrt{6}}-\frac{\sin\phi}{\sqrt{2}} & \frac{1}{\sqrt{3}} \\ \frac{2\sin\phi}{\sqrt{6}} & \frac{2\cos\phi}{\sqrt{6}} & \frac{1}{\sqrt{3}} \\ -\frac{\cos\phi}{\sqrt{2}}-\frac{\sin\phi}{\sqrt{6}} & -\frac{\cos\phi}{\sqrt{6}}+\frac{\sin\phi}{\sqrt{2}} & \frac{1}{\sqrt{3}} \end{pmatrix}, \tag{16}$$

maps the z direction to $[111]$ (which is parallel to the light propagation direction $\hat{\mathbf{k}}$) and the xy plane to (111), with a variable angle ϕ. Consider the case where the static magnetic field is applied parallel to the x' direction. It is assumed that $M'_1\simeq M_0$, $M'_2/M_0\equiv\mu_2\ll 1$ and $M'_3/M_0\equiv\mu_3\ll 1$, where M_0 is the saturation magnetization.

In the truncation approximation, the transverse dielectric tensor is taken to be the 2×2 upper left block of the 3×3 tensor ε'. Moreover, the terms independent on $Q_{\rm s}$, μ_2 and μ_3 are disregarded. In this approximation, $\varepsilon'-\varepsilon_{\rm r}$ is represented by a 2×2 matrix given by $M_0^2(\mu_3\mathbf{a}'+\mu_2\mathbf{a}'')\cdot\boldsymbol{\sigma}$, where $\mathbf{a}'$ ($\mathbf{a}''$) is the real (imaginary) part of the vector $\mathbf{a}=\mathbf{a}'+i\mathbf{a}''$, which is given by (to first order in $Q_{\rm s}$)

$$\mathbf{a}=-\frac{\sqrt{2}g}{3}\left(\cos 3\phi-\frac{3i\left(\frac{1}{3}+\frac{2g_{44}}{g}\right)}{\sqrt{2}},\frac{3Q_{\rm s}}{\sqrt{2}M_0 g},\sin 3\phi\right), \tag{17}$$

and where $\boldsymbol{\sigma}$ is the Pauli matrix vector [see Equation (1)]. Alternatively,

$$\varepsilon'-\varepsilon_{\rm r}=\frac{M_0^2}{2}(\mu_+\mathbf{a}^*+\mu_-\mathbf{a})\cdot\boldsymbol{\sigma}\,, \tag{18}$$

where $\mu_\pm=\mu_3\pm i\mu_2$.

The Hermitian matrices $(\mathbf{a}''\times\mathbf{a}')\cdot\boldsymbol{\sigma}$, $S^\dagger S$ and $SS^\dagger$, where $S=\mathbf{a}\cdot\boldsymbol{\sigma}$ (see Equation (18)), share the same eigenvectors, which are denoted by $|\mathbf{a}_+\rangle$ and $|\mathbf{a}_-\rangle$. The transformed matrix $\tilde{S}=U^{-1}SU$, where U is the 2×2 unitary transformation matrix corresponding to the basis $\{|\mathbf{a}_+\rangle,|\mathbf{a}_-\rangle\}$, has a hollow form (see Equation (6.150) of Ref. [62]). The matrix representation of $\varepsilon'-\varepsilon_{\rm r}$ in that basis, which is denoted by $\varepsilon_{\rm h}$, is given by

$$\varepsilon_{\rm h}=\frac{M_0^2}{2}\begin{pmatrix} 0 & \mu_-\zeta_1+\mu_+\zeta_2^* \\ \mu_-\zeta_2+\mu_+\zeta_1^* & 0 \end{pmatrix}, \tag{19}$$

where $\zeta_1\zeta_2=\mathbf{a}\cdot\mathbf{a}$, $|\zeta_1|^2+|\zeta_2|^2=2\mathbf{a}\cdot\mathbf{a}^*$, and $|\zeta_2|^2-|\zeta_1|^2=4|\mathbf{a}''\times\mathbf{a}'|$.

Both scattering selection rules and sideband asymmetry (between Stokes and anti-Stokes) can be characterized in terms of the ratio $\zeta_{\mathbf{a}}$, which is defined by (see Equation (19), and note that $|\zeta_{\mathbf{a}}|\le 1$)

$$\zeta_{\mathbf{a}}=\frac{|\zeta_2|^2-|\zeta_1|^2}{|\zeta_1|^2+|\zeta_2|^2}=\frac{2|\mathbf{a}''\times\mathbf{a}'|}{|\mathbf{a}'|^2+|\mathbf{a}''|^2}\,. \tag{20}$$

Note that sideband asymmetry is possible only when $|\mathbf{a}''\times\mathbf{a}'|>0$ (see Equations (19) and (20)). For radio and optical communication, it is well known that sideband asymmetry is impossible when only the amplitude, or only the frequency, or only the phase is modulated by a monochromatic signal. Moreover, with simultaneously applied two different modulation methods, sideband asymmetry becomes possible only when one modulation method is phase-shifted with respect to the other. These properties are all reflected by the condition $|\mathbf{a}''\times\mathbf{a}'|>0$.

For YIG, $(Q_{\rm s}/(M_0 g))^2=44.2$, and $2g_{44}/g=-4.0$ [20]; hence, $\zeta_{\mathbf{a}}\simeq 0.84$ (see Equations (17) and (20), and note that the term $\sin^2 3\phi$ has a relatively small effect). The largest sideband asymmetry is obtained for input states $|\mathbf{a}_+\rangle$ and $|\mathbf{a}_-\rangle$ (eigenvectors of

$(\mathbf{a}'' \times \mathbf{a}') \cdot \sigma$). As can be seen from Equation (17), for YIG, the vector $\mathbf{a}'' \times \mathbf{a}'$ is nearly parallel to the unit vector $\hat{\mathbf{z}}$.

The intensities of both the left (shorter wavelength, anti-Stokes) and right (longer wavelength, Stokes) sidebands can be manipulated using the PC shown in Figure 2a, which controls the input SOP. The vector of the three voltages controlling this PC are denoted by $\mathbf{V}_{\mathrm{PC}} = (V_{\mathrm{PC},1}, V_{\mathrm{PC},2}, V_{\mathrm{PC},3})$. A searching procedure is implemented to determine the value $\mathbf{V}_{\mathrm{PC,L}}$ ($\mathbf{V}_{\mathrm{PC,R}}$), for which the intensity of the left (right) sideband, which is denoted by I_{L} (I_{R}), is maximized. The measurements shown in Figure 3 are performed with values of $\mathbf{V}_{\mathrm{PC}}$ given by $\mathbf{V}_{\mathrm{PC}} = v\mathbf{V}_{\mathrm{PC,L}} + (1-v)\mathbf{V}_{\mathrm{PC,R}}$, where $0 \leq v \leq 1$. The Poincaré vector $\mathbf{P} = (P_1, P_2, P_3)$ can be extracted from the POSA data using the method discussed in Section 2. The Poincaré vectors $\mathbf{P}$ are shown in Figure 3 for three different values of the parameter v, which are indicated in Figure 3(1,3) by the letters a, b, and c. The numbers 1, 2, and 3 in the Poincaré plots' labels in Figure 3 refer to the left sideband, central peak, and right sideband, respectively.

A value for the asymmetry parameter given by $\zeta_{\mathbf{a}} = 0.92$ is extracted from the data shown in Figure 3(1,3). This result suggests that the above-discussed theoretical analysis underestimates $\zeta_{\mathbf{a}}$ (recall that the calculated value is 0.84) [44]. The disagreement in the SOP between the theory and the experiment is quantified by the parameter $\delta_{\mathrm{P}} = \|\mathbf{P}_{\mathrm{E}} - \mathbf{P}_{\mathrm{T}}\| / \|\mathbf{P}_{\mathrm{T}}\|$, where $\mathbf{P}_{\mathrm{E}}$ denotes a measured Poincaré vector, and $\mathbf{P}_{\mathrm{T}}$ is theoretically derived using Equation (19). For the data shown in Figure 3 $\delta_{\mathrm{P}} \lesssim 0.13$. The disagreement is partially attributed to magneto-dichroism (i.e., polarization-dependent absorption), which is theoretically disregarded. Further study is needed to explore the effect of magneto-dichroism and other possible mechanisms contributing to the observed disagreement.

5. USOC

USOC formation in a cryogenic fiber loop laser has been recently demonstrated [10,52]. The USOC can be employed as a tunable multi-mode lasing source [63]. Multimode lasing has a variety of applications in the fields of sensing, spectroscopy, signal processing, and communication. Multimode lasing in the telecom band has been demonstrated by integrating Erbium doped fibers (EDF) cooled by liquid nitrogen into a fiber ring laser [64–67]. It has been recently proposed that EDF operating at low temperatures can be used for storing quantum information [68–72]. For some USOC-based applications, DOP specification is important. As is discussed below, the POSA high spectral resolution allows such a specification for individual USOC peaks.

A sketch of the cryogenic fiber loop laser used for studying USOC is shown in Figure 2b. The loop is made of an undoped single mode fiber (Corning 28) and a 5 m long EDF, which is used for optical amplification. The EDF has an absorption of 30 dB m^{-1} at 1530 nm and a mode field diameter of 6.5 μm at 1550 nm. The cold EDF is integrated with a room temperature fiber loop using a wavelength-division multiplexing (WDM) device. The EDF is pumped using a 980 nm laser diode (LD) biased with the current denoted by I_{D}. A 10:90 OC and two isolators (labeled by arrows in the sketch shown in Figure 2b) are integrated into the fiber loop. The output port of the 10:90 OC is connected to the POSA setup shown in Figure 1b.

The plot in Figure 4a shows the total POSA signal intensity $I_+ + I_-$ as a function of the TL2 wavelength λ in the band where the USOC is formed (1539.7–1541.5 nm). The underlying mechanism responsible for USOC formation has remained mainly unknown [10,52]. The POSA is employed to determine the DOP of each USOC peak. The result, which is shown in Figure 4b, reveals that the first (shortest wavelength) USOC peak has the largest DOP. Note that commonly in fiber lasers, the DOP is below about 0.15, unless a polarization-maintaining fiber is used [73]. Further study is needed to explore how a higher USOC DOP, which is needed for some applications, can be achieved.

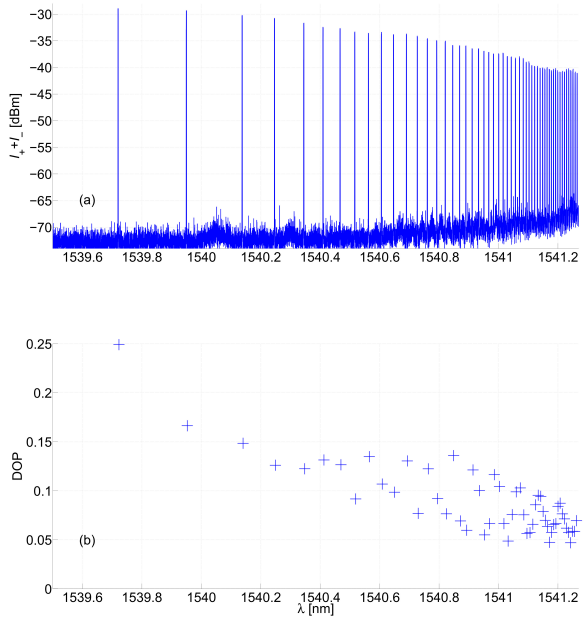


Figure 4. USOC intensity (**a**) and DOP (**b**). The diode current is 0.2 A, and the EDF temperature is 3.2 K.

6. Discussion and Summary

A variety of POSA configurations have been developed and optimized for specific applications [74]. Commonly, wavelength separation in POSA instruments is achieved by integrating either a diffraction grating or a tunable optical filter. For some applications, in fields including astronomy and mineralogy analysis [75], these methods provide sufficiently high spectral resolution. However, a much higher spectral resolution can be achieved by implementing the method of coherent heterodyne detection [2–4].

Our coherent POSA setup operates in the entire C band (1530–1565 nm), and it has a dynamic range of about 70 dB. It allows SOP measurement with a spectral resolution of 5 MHz (corresponding wavelength resolution of 0.04 pm in the telecom band). The SOP can be alternatively measured by combining a polarimeter with a tunable optical filter. The filter-based method is simpler to implement; however, its spectral resolution is limited by the ratio between the filter's FSR and finesse. Filter-based SOP measurements of a driven FMSR have been reported in [8,44]. In that study, the FMSR resonance frequency $\omega_m/(2\pi)$ was tuned close to 7 GHz, and a scanning Fabry–Pérot etalon having an FSR of 10 GHz (corresponding wavelength spacing of 80 pm in the telecom band) was employed as a tunable filter [8,44]. Accurate SOP measurements of a driven FMSR can be obtained provided that the filter is capable of resolving individual sidebands. This task is challenging for a driven FMSR, because the power carried by both Stokes and anti-Stokes optical sidebands is commonly at least three orders of magnitude smaller than the power carried by the pump tone (see Figure 3(2)). Thus, for the SOP measurements of a driven FMSR, the much higher spectral resolution offered by the coherent POSA significantly improves the accuracy. For the USOC, as can be seen from Figure 4a, the spacing between peaks is far too small to practically allow any accurate SOP measurements using the filter-based method.

Future work will be devoted to optimize some applications that are based on the optical systems under study. For the FMSR modulator, ways to further increase the asymmetry parameter $\zeta_{\mathbf{a}}$ will be explored to allow more efficient optical communication based on the SSM. Moreover, ways to enhance the USOC DOP will be investigated in order to open the way for some novel applications that require a multi-mode lasing source having a high level of intermode coherency.

Funding: This work was supported by the Technion security research foundation.

Institutional Review Board Statement: No applicable.

Informed Consent Statement: No applicable.

Data Availability Statement: Data are contained within the article.

Conflicts of Interest: The authors declare no conflict of interest.

References

1. Goldstein, D.H. *Polarized Light*; CRC Press: Boca Raton, FL, USA, 2017.
2. Yao, X.S.; Zhang, B.; Chen, X.; Willner, A.E. Real-time optical spectrum analysis of a light source using a polarimeter. *Opt. Express* **2008**, *16*, 17854–17863. [CrossRef]
3. Kim, E.; Dave, D.; Milner, T.E. Fiber-optic spectral polarimeter using a broadband swept laser source. *Opt. Commun.* **2005**, *249*, 351–356. [CrossRef]
4. Kim, H.K.; Kim, S.K.; Park, H.G.; Kim, B.Y. Polarimetric fiber laser sensors. *Opt. Lett.* **1993**, *18*, 317–319. [CrossRef] [PubMed]
5. Baney, D.M.; Szafraniec, B.; Motamedi, A. Coherent optical spectrum analyzer. *IEEE Photonics Technol. Lett.* **2002**, *14*, 355–357. [CrossRef]
6. Feng, K.; Cui, J.; Dang, H.; Wu, W.; Sun, X.; Jiang, X.; Tan, J. An optoelectronic equivalent narrowband filter for high resolution optical spectrum analysis. *Sensors* **2017**, *17*, 348. [CrossRef] [PubMed]
7. Dang, H.; Liu, H.; Cheng, L.; Tian, Y.; Chen, J.; Feng, K.; Cui, J.; Shum, P.P. Deconvolutional suppression of resolution degradation in coherent optical spectrum analyzer. *J. Light. Technol.* **2023**, *13*, 4430. [CrossRef]
8. Haigh, J.A.; Nunnenkamp, A.; Ramsay, A.J.; Ferguson, A.J. Triple-resonant brillouin light scattering in magneto-optical cavities. *Phys. Rev. Lett.* **2016**, *117*, 133602. [CrossRef] [PubMed]
9. Chai, C.Z.; Shen, Z.; Zhang, Y.L.; Zhao, H.Q.; Guo, G.C.; Zou, C.L.; Dong, C.H. Single-sideband microwave-to-optical conversion in high-q ferrimagnetic microspheres. *Photonics Res.* **2022**, *10*, 820–827. [CrossRef]
10. Buks, E. Low temperature spectrum of a fiber loop laser. *Phys. Lett. A* **2023**, *458*, 128591. [CrossRef]
11. Potton, R.J. Reciprocity in optics. *Rep. Prog. Phys.* **2004**, *67*, 717. [CrossRef]
12. Rameshti, B.Z.; Kusminskiy, S.V.; Haigh, J.A.; Usami, K.; Lachance-Quirion, D.; Nakamura, Y.; Hu, C.; Tang, H.X.; Bauer, G.E.W.; Blanter, Y.M. Cavity magnonics. *Phys. Rep.* **2022**, *979*, 1–61. [CrossRef]
13. Kusminskiy, S.V. Cavity optomagnonics. In *Optomagnonic Structures: Novel Architectures for Simultaneous Control of Light and Spin Waves*; World Scientific: Singapore, 2021; pp. 299–353.
14. Zhu, N.; Zhang, X.; Han, X.; Zou, C.; Tang, H.X. Inverse faraday effect in an optomagnonic waveguide. *arXiv* **2020**, arXiv:2012.11119.
15. Juraschek, D.M.; Wang, D.S.; Narang, P. Sum-frequency excitation of coherent magnons. *Phys. Rev. B* **2021**, *103*, 094407. [CrossRef]
16. Bittencourt, V.A.S.V.; Liberal, I.; Kusminskiy, S.V. Light propagation and magnon-photon coupling in optically dispersive magnetic media. *Phys. Rev. B* **2022**, *105*, 014409. [CrossRef]
17. Zhang, X.; Zhu, N.; Zou, C.; Tang, H.X. Optomagnonic whispering gallery microresonators. *Phys. Rev. Lett.* **2016**, *117*, 123605. [CrossRef] [PubMed]
18. der Ziel, J.P.V.; Pershan, P.S.; Malmstrom, L.D. Optically-induced magnetization resulting from the inverse faraday effect. *Phys. Rev. Lett.* **1965**, *15*, 190. [CrossRef]
19. Zheng, S.; Wang, Z.; Wang, Y.; Sun, F.; He, Q.; Yan, P.; Yuan, H.Y. Tutorial: Nonlinear magnonics. *arXiv* **2023**, arXiv:2303.16313.
20. Stancil, D.D.; Prabhakar, A. *Spin Waves*; Springer: Berlin/Heidelberg, Germany, 2009.
21. Oraevsky, A.N. Whispering-gallery waves. *Quantum Electron.* **2002**, *32*, 377. [CrossRef]
22. Schunk, G.; Fürst, J.U.; Förtsch, M.; Strekalov, D.V.; Vogl, U.; Sedlmeir, F.; Schwefel, H.G.L.; Leuchs, G.; Marquardt, C. Identifying modes of large whispering-gallery mode resonators from the spectrum and emission pattern. *Opt. Express* **2014**, *22*, 30795–30806. [CrossRef]
23. Gorodetsky, M.L.; Fomin, A.E. Geometrical theory of whispering-gallery modes. *IEEE J. Sel. Top. Quantum Electron.* **2006**, *12*, 33–39. [CrossRef]
24. Walker, L.R. Magnetostatic modes in ferromagnetic resonance. *Phys. Rev.* **1957**, *105*, 390. [CrossRef]
25. Osada, A.; Gloppe, A.; Nakamura, Y.; Usami, K. Orbital angular momentum conservation in brillouin light scattering within a ferromagnetic sphere. *New J. Phys.* **2018**, *20*, 103018. [CrossRef]
26. Osada, A.; Hisatomi, R.; Noguchi, A.; Tabuchi, Y.; Yamazaki, R.; Usami, K.; Sadgrove, M.; Yalla, R.; Nomura, M.; Nakamura, Y. Cavity optomagnonics with spin-orbit coupled photons. *Phys. Rev. Lett.* **2016**, *116*, 223601. [CrossRef] [PubMed]
27. Sharma, S.; Blanter, Y.M.; Bauer, G.E.W. Light scattering by magnons in whispering gallery mode cavities. *Phys. Rev. B* **2017**, *96*, 094412. [CrossRef]
28. Sharma, S.; Blanter, Y.M.; Bauer, G.E.W. Optical cooling of magnons. *Phys. Rev. Lett.* **2018**, *121*, 087205. [CrossRef] [PubMed]
29. Almpanis, E. Dielectric magnetic microparticles as photomagnonic cavities: Enhancing the modulation of near-infrared light by spin waves. *Phys. Rev. B* **2018**, *97*, 184406. [CrossRef]

30. Zivieri, R.; Vavassori, P.; Giovannini, L.; Nizzoli, F.; Fullerton, E.E.; Grimsditch, M.; Metlushko, V. Stokes–anti-stokes brillouin intensity asymmetry of spin-wave modes in ferromagnetic films and multilayers. *Phys. Rev. B* **2002**, *65*, 165406. [CrossRef]
31. Desormiere, B.; Gall, H.L. Interaction studies of a laser light with spin waves and magnetoelastic waves propagating in a yig bar. *IEEE Trans. Magn.* **1972**, *8*, 379–381. [CrossRef]
32. Liu, Z.; Wang, B.; Xiong, H.; Wu, Y. Magnon-induced high-order sideband generation. *Opt. Lett.* **2018**, *43*, 3698–3701. [CrossRef] [PubMed]
33. Zhu, N.; Zhang, X.; Han, X.; Zou, C.; Zhong, C.; Wang, C.; Jiang, L.; Tang, H.X. Waveguide cavity optomagnonics for microwave-to-optics conversion. *Optica* **2020**, *7*, 1291–1297. [CrossRef]
34. Li, J.; Wang, Y.; Wu, W.; Zhu, S.; You, J.Q. Quantum network with magnonic and mechanical nodes. *PRX Quantum* **2021**, *2*, 040344. [CrossRef]
35. Nayak, B.K.; Buks, E. Polarization-selective magneto-optical modulation. *J. Appl. Phys.* **2022**, *132*, 193905. [CrossRef]
36. Liu, Z.X.; Xiong, H. Magnon laser based on brillouin light scattering. *Opt. Lett.* **2020**, *45*, 5452–5455. [CrossRef] [PubMed]
37. Sandercock, J.R.; Wettling, W. Light scattering from thermal acoustic magnons in yttrium iron garnet. *Solid State Commun.* **1973**, *13*, 1729–1732. [CrossRef]
38. Hu, H.L.; Morgenthaler, F.R. Strong infrared-light scattering from coherent spin waves in yttrium iron garnet. *Appl. Phys. Lett.* **1971**, *18*, 307–310. [CrossRef]
39. Ghasemian, E. Dissipative dynamics of optomagnonic nonclassical features via anti-stokes optical pulses: Squeezing, blockade, anti-correlation, and entanglement. *Sci. Rep.* **2023**, *13*, 12757. [CrossRef] [PubMed]
40. Kusminskiy, S.V.; Tang, H.X.; Marquardt, F. Coupled spin-light dynamics in cavity optomagnonics. *Phys. Rev. A* **2016**, *94*, 033821. [CrossRef]
41. Wettling, W.; Cottam, M.G.; Sandercock, J.R. The relation between one-magnon light scattering and the complex magneto-optic effects in yig. *J. Phys. Solid State Phys.* **1975**, *8*, 211. [CrossRef]
42. Cottam, M.G.; Lockwood, D.J. *Light Scattering in Magnetic Solids*; Wiley: New York, NY, USA, 1986.
43. Liu, T.; Zhang, X.; Tang, H.X.; Flatté, M.E. Optomagnonics in magnetic solids. *Phys. Rev. B* **2016**, *94*, 060405. [CrossRef]
44. Haigh, J.A.; Nunnenkamp, A.; Ramsay, A.J. Polarization dependent scattering in cavity optomagnonics. *Phys. Rev. Lett.* **2021**, *127*, 143601. [CrossRef]
45. Hisatomi, R.; Noguchi, A.; Yamazaki, R.; Nakata, Y.; Gloppe, A.; Nakamura, Y.; Usami, K. Helicity-changing brillouin light scattering by magnons in a ferromagnetic crystal. *Phys. Rev. Lett.* **2019**, *123*, 207401. [CrossRef] [PubMed]
46. Hisatomi, R.; Osada, A.; Tabuchi, Y.; Ishikawa, T.; Noguchi, A.; Yamazaki, R.; Usami, K.; Nakamura, Y. Bidirectional conversion between microwave and light via ferromagnetic magnons. *Phys. Rev. B* **2016**, *93*, 174427. [CrossRef]
47. Wu, W.J.; Wang, Y.P.; Wu, J.Z.; Li, J.; You, J.Q. Remote magnon entanglement between two massive ferrimagnetic spheres via cavity optomagnonics. *Phys. Rev. A* **2021**, *104*, 023711. [CrossRef]
48. Lazzarini, V.; Timoney, J.; Lysaght, T. Asymmetric-spectra methods for adaptive fm synthesis. In Proceedings of the DAFX-08 the 11th Int. Conference on Digital Audio Effects, Espoo, Helsinki, Finland, 1–4 September 2008.
49. Li, W.; Wang, W.T.; Wang, L.X.; Zhu, N.H. Optical vector network analyzer based on single-sideband modulation and segmental measurement. *IEEE Photonics J.* **2014**, *6*, 1–8. [CrossRef]
50. Shimotsu, S.; Oikawa, S.; Saitou, T.; Mitsugi, N.; Kubodera, K.; Kawanishi, T.; Izutsu, M. Single side-band modulation performance of a linbo 3 integrated modulator consisting of four-phase modulator waveguides. *IEEE Photonics Technol. Lett.* **2001**, *13*, 364–366. [CrossRef] [PubMed]
51. Onbasli, M.C.; Beran, L.; Zahradník, M.; Kučera, M.; Antoš, R.; Mistrík, J.; Dionne, G.F.; Veis, M.; Ross, C.A. Optical and magneto-optical behavior of cerium yttrium iron garnet thin films at wavelengths of 200–1770 nm. *Sci. Rep.* **2016**, *6*, 23640. [CrossRef] [PubMed]
52. Buks, E. Intermode coupling in a fiber loop laser at low temperatures. *J. Light. Technol.* **2024**, *42*, 2951. [CrossRef]
53. Fletcher, P.C.; Bell, R.O. Ferrimagnetic resonance modes in spheres. *J. Appl. Phys.* **1959**, *30*, 687–698. [CrossRef]
54. Sharma, S. Cavity Optomagnonics: Manipulating Magnetism by Light. Ph.D. Thesis, Delft University of Technology, Delft, The Netherlands, 2019.
55. Jin, T.L. Design of a Yig-Tuned Oscillator. Master's Thesis, New Jersey Institute of Technology, Newark, NJ, USA, 1974.
56. Freiser, M. A survey of magnetooptic effects. *IEEE Trans. Magn.* **1968**, *4*, 152–161. [CrossRef]
57. Boardman, A.D.; Xie, M. Magneto-optics: A critical review. *Introd. Complex Mediu. Opt. Electromagn.* **2003**, *123*, 197.
58. Boardman, A.D.; Velasco, L. Gyroelectric cubic-quintic dissipative solitons. *IEEE J. Sel. Top. Quantum Electron.* **2006**, *12*, 388–397. [CrossRef]
59. Wood, D.L.; Remeika, J.P. Effect of impurities on the optical properties of yttrium iron garnet. *J. Appl. Phys.* **1967**, *38*, 1038–1045. [CrossRef]
60. Prokhorov, A.M.; Smolenskiĭ, G.A.; Ageev, A.N. Optical phenomena in thin-film magnetic waveguides and their technical application. *Sov. Phys. Uspekhi* **1984**, *27*, 339. [CrossRef]
61. Prabhakar, A.; Stancil, D.D. *Spin Waves: Theory and Applications*; Springer: Berlin/Heidelberg, Germany, 2009; Volume 5.
62. Buks, E. Quantum Mechanics–Lecture Notes. 2024. Available online: http://buks.net.technion.ac.il/teaching/ (accessed on 10 May 2024)
63. Buks, E. Tunable multimode lasing in a fiber ring. *Phys. Rev. Appl.* **2023**, *19*, L051001. [CrossRef]

64. Yamashita, S.; Hotate, K. Multiwavelength erbium-doped fibre laser using intracavity etalon and cooled by liquid nitrogen. *Electron. Lett.* **1996**, *32*, 1298–1299. [CrossRef]
65. Liu, H.; He, W.; Liu, Y.; Dong, Y.; Zhu, L. Erbium-doped fiber laser based on femtosecond laser inscribed fbg through fiber coating for strain sensing in liquid nitrogen environment. *Opt. Fiber Technol.* **2022**, *72*, 102988. [CrossRef]
66. Lopez, J.; Kerbertt, H.; Plata, M.; Hernandez, E.; Stepanov, S. Two-wave mixing in erbium-doped-fibers with spectral-hole burning at 77k. *J. Opt.* **2020**, *22*, 085401. [CrossRef]
67. Gouët, J.L.; Oudin, J.; Perrault, P.; Abbes, A.; Odier, A.; Dubois, A. On the effect of low temperatures on the maximum output power of a coherent erbium-doped fiber amplifier. *J. Light. Technol.* **2019**, *37*, 3611–3619. [CrossRef]
68. Wei, S.; Jing, B.; Zhang, X.; Liao, J.; Li, H.; You, L.; Wang, Z.; Wang, Y.; Guang-Wei, D.; Song, H.; et al. Storage of 1650 modes of single photons at telecom wavelength. *arXiv* **2022**, arXiv:2209.00802.
69. Ortu, A.; Rakonjac, J.V.; Holzäpfel, A.; Seri, A.; Grandi, S.; Mazzera, M.; de Riedmatten, H.; Afzelius, M. Multimode capacity of atomic-frequency comb quantum memories. *Quantum Sci. Technol.* **2022**, *7*, 035024. [CrossRef]
70. Liu, D.C.; Li, P.Y.; Zhu, T.X.; Zheng, L.; Huang, J.Y.; Zhou, Z.Q.; Li, C.F.; Guo, G.C. On-demand storage of photonic qubits at telecom wavelengths. *arXiv* **2022**, arXiv:2201.03692.
71. Veissier, L.; Falamarzi, M.; Lutz, T.; Saglamyurek, E.; Thiel, C.W.; Cone, R.L.; Tittel, W. Optical decoherence and spectral diffusion in an erbium-doped silica glass fiber featuring long-lived spin sublevels. *Phys. Rev. B* **2016**, *94*, 195138. [CrossRef]
72. Shafiei, S.; Saglamyurek, E.; Oblak, D. Hour-long decay-time of erbium spins in an optical fiber at milli-kelvin temperatures. In Proceedings of the Quantum Information and Measurement 2021, Washington, DC, USA, 1–5 November 2021; p. F2A–4.
73. Liem, A.; Limpert, J.; Schreiber, T.; Reich, M.; Zellmer, H.; Tunnermann, A.; Carter, A.; Tankala, K. High power linearly polarized fiber laser. In Proceedings of the Conference on Lasers and Electro-Optics, San Francisco, CA, USA, 16–21 May 2004; p. CMS4.
74. Trujillo-Bueno, J.; Moreno-Insertis, F.; Sánchez, F. *Astrophysical Spectropolarimetry*; Cambridge University Press: Cambridge, UK, 2002.
75. Belyaev, D.A.; Yushkov, K.B.; Anikin, S.P.; Dobrolenskiy, Y.S.; Laskin, A.; Mantsevich, S.N.; Molchanov, V.Y.; Potanin, S.A.; Korablev, O.I. Compact acousto-optic imaging spectro-polarimeter for mineralogical investigations in the near infrared. *Opt. Express* **2017**, *25*, 25980–25991. [CrossRef] [PubMed]

Disclaimer/Publisher's Note: The statements, opinions and data contained in all publications are solely those of the individual author(s) and contributor(s) and not of MDPI and/or the editor(s). MDPI and/or the editor(s) disclaim responsibility for any injury to people or property resulting from any ideas, methods, instructions or products referred to in the content.